J Nanopart Res (2020) 22: 74
https://doi.org/10.1007/s11051-020-04783-0

RESEARCH PAPER

Synthesis of gold-coated branched ZnO nanorods for gas sensor fabrication

Ameen Thamer · Abdulqader Faisal · Ali Abed · Wafaa Khalef

Received: 26 August 2019 / Accepted: 13 February 2020 / Published online: 18 March 2020

Abstract In this work, atypical zinc oxide nanorods (ZnO NRs) on quartz substrates were successfully synthesized using simple, low-cost, and environmentally friendly hydrothermal method. The ZnO NRs were grown on a pre-seeded seed layer of ZnO nanocrystals using the spin coating process. Gold nanoparticles (Au NPs) were sputtered on the ZnO NRs film. The structure and morphology of the produced nanostructures were characterized by X-ray diffraction (XRD) and scanning electron microscope (SEM). The XRD analysis revealed that the ZnO NRs were single crystalline with hexagonal wurtzite structure grown with preferred orientation of (002). The SEM morphology shows a semi-hierarchical ZnO NRs with an estimated diameter of 200–400 nm and length of 4–5 μm. The optical properties of the ZnO NRs film were investigated using UV-visible spectrophotometers. The obtained bandgap of ZnO film was 3.0 eV. Electrical and thermal properties were also measured. The resistance changes versus temperature variation of ZnO NRs were given a semiconductor behavior. The gas sensor was fabricated based on bare ZnO NRs and Au NPs/ZnO NRs hybrid. The second nanostructure exhibited an enhanced sensor sensitivity toward ethanol gas at an optimized working temperature of 325 °C.

Keywords Nanoparticles · Bare ZnO NRs · Gold-decorated ZnO NRs · Energy bandgap · ZnO seed layer · Ethanol vapor sensor enhancement

A. Thamer
Production Engineering and Metallurgy Department, University of Technology, Baghdad, Iraq

A. Faisal (✉) · W. Khalef
Applied Science Department, University of Technology, Baghdad, Iraq
e-mail: Abdulf330@gmail.com

A. Abed
Nanotechnology and Advanced Material Research Center, University of Technology, Baghdad, Iraq

Introduction

Zinc oxide (ZnO) is an important semiconductor material and shows unique physical and chemical properties (Yuhai et al. 2016). ZnO has a wide bandgap with a direct energy gap of 3.37 eV and exciton binding energy of 60 meV at room temperature (300 K). Therefore, it has been used for many applications such as photovoltaic cells (Benoit et al. 2011), dye-sensitized solar cells (Lin et al. 2012), photocatalyst (Zhai and Huang 2016), field emission (Huanming et al. 2017), lithium-ion battery (Changlei et al. 2016), biomedical applications (Hamed and Majid 2017), gas sensors (Faisal 2017), temperature and humidity sensor (Mohamad et al. 2015), and temperature sensor (Richa 2013). ZnO nanostructures have been grown by many different techniques such as chemical vapor deposition (CVD) (Faisal 2016), RF magnetron sputtering (Husam and Abdullah 2015), electron beam evaporation (Giri et al. 2007), physical vapor deposition (PVD) (Jimenez-Cadena et al. 2010), pulsed laser deposition (Rajesh et al. 2014), thermal oxidation (Alejandro et al. 2016;

Mohammad et al. 2012), spray pyrolysis (Muchuweni et al. 2017), sol-gel technique (Hasnidawani et al. 2016), chemical bath deposition (Zhiwei and Amy 2015), thermal evaporation (Lv et al. 2010), solvothermal (Doungporn et al. 2009), precipitation (Kołodziejczak-Radzimska et al. 2010), and hydrothermal route (Shi et al. 2013). The hydrothermal route is the preferred technique among those due to it being simple and inexpensive, which does not require expensive machines such as high vacuum and high-temperature furnaces. ZnO exhibits a great diversity of morphologies such as nanoparticles (Ayesha et al. 2017), nanoflowers (Muhammad et al. 2016), nanowires (Yangyang et al. 2012), comb-like nanostructures (Faisal 2017), nanosheet (Xiaohong et al. 2016), nanotubes (Yang et al. 2009), and nanorods (Salvatore et al. 2017).

In the present work, we carried on a low-cost hydrothermal growth to synthesize ZnO NRs on a quartz substrate. The morphology of ZnO nanostructures with seed layer preparation via a spin coating process was investigated. The nanostructure materials as synthesized with and without Au coating were fabricated as gas sensors for ethanol at room temperature and optimized temperature of 325 °C. The sensing enhancement was also investigated with gold nanoparticle–decorated ZnO nanostructures.

The experimental section

ZnO seed layer preparation

The nanocrystals of the ZnO seed layer prepared on quartz substrates were carried out by the spin coating technique. The ZnO seed layer solution was made by dissolving 10 mM of zinc acetate [(Zn (CH3COO) 2.2H2O] in 20 ml of absolute ethyl alcohol. The result was then sonicated for 1 h. Prior to the solution growth procedures, the substrates were sequentially and repeatedly immersed in isopropanol under sonication for 15 min to get rid of organic contaminants. This cleaning step is accompanied each time by rinsing the substrates in deionized (DI) water, and finally, the substrates were blown dry by nitrogen gun and dried in air at room temperature (RT). In a typical process, the seed layer was spun coated three times with a seed solution (ZnO nanoparticles) at 3000 rotations per min (RPM) for the 30 s and then the samples were annealed in a preheated oven at 120 °C for 10 s. This process was repeated for 5 times. The coated substrates were then annealed at a temperature of 350 °C for 60 min for ZnO nanocrystals formation. The primary benefits of using ZnO nanoparticles as the seed layer in the hydrothermal growth method are to provide nucleation sites for ZnO nanorods. Likewise, the ZnO seed layer was found to be a vital factor for the alignment and uniformity of the grown ZnO nanorods (Alaie et al. 2016).

ZnO nanorods growth process

The ZnO nanostructures were grown on the previously coated seed layers of quartz substrates via the hydrothermal route**.** The growth solution was prepared by dissolving 25 mM of zinc nitrate [Zn $(NO_3)_2.6H_2O$] and 25 mM of hexamethylenetetramine (HMT/$C_6H_{12}N_4$) in 200 ml of deionized (DI) water. The solution was sonicated for 30 min to ensure good homogeneity. The pre-cleaned quartz substrates are then fixed vertically on a slotted Teflon block and immersed into the growth solution as shown in Fig. 1. This was transferred into an oven to start the growth process at a temperature of 90 °C and time for 4 h. At the end of this process, the substrates were removed from the solution, washed with DI for several times, and dried at room temperature.

Characterization

The crystalline structure of ZnO NRs was characterized by using Shimadzu XRD – 6000/Japan – diffractometer equipped with Cu K_α radiation ($\lambda = 1.5406$ Å) employing a scanning rate of 10 deg/min and 2θ ranges from 30° to 80°. The morphology of the product was

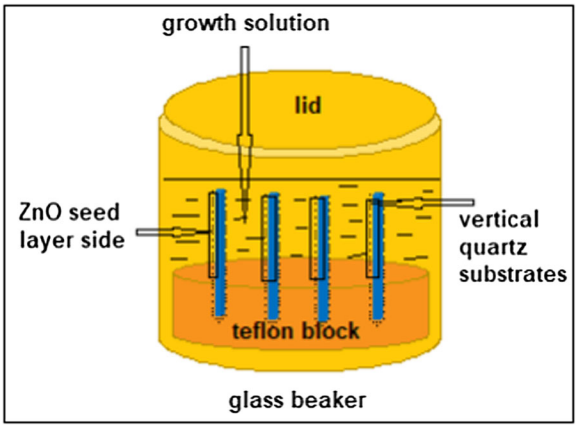

Fig. 1 Hydrothermal growth cell of ZnO nanostructure

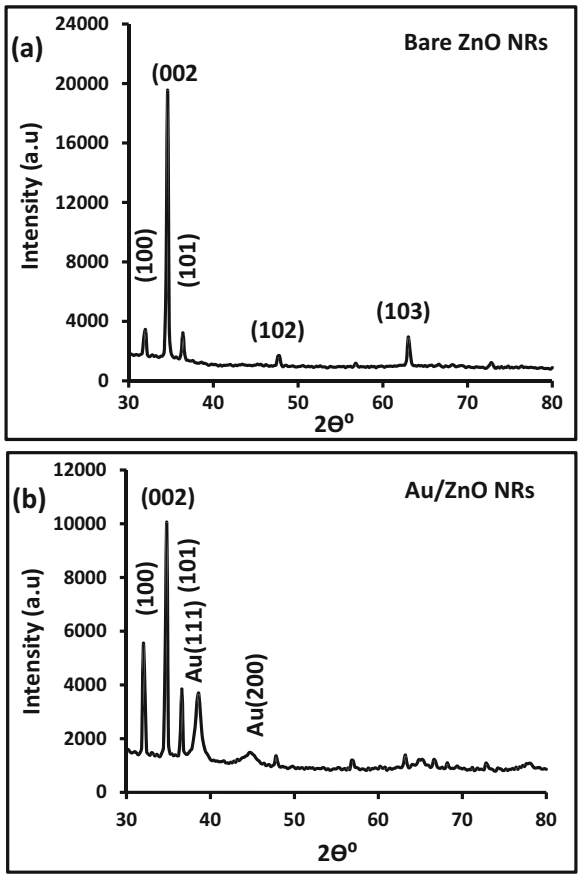

Fig. 2 XRD spectrum of **a** bare ZnO NRs and **b** Au/ZnO NRs on a quartz substrate

observed with a scanning electron microscope (SEM model Tescan Vega II-Cheek, Netherlands). The optical transmittance of the ZnO was measured using Shimadzu/UV-visible-2450 spectrophotometer.

Results and discussion

Crystal structure and morphology analysis

XRD analysis

The XRD analysis shown in Fig. 2 was conducted at the 2θ range of 30–80°. Figure 2a shows the XRD pattern of the as-synthesized ZnO NRs. The observed diffraction peaks appeared at 32.80° (100), 34.60° (002), 36.40° (101), 48.20° (102), and 63.50° (103), which are well matched with the JCPDS card No. 36-1451. The observation of these peaks suggests that the material is a pure ZnO phase.

The XRD pattern of Au/ZnO NRs film is shown in Fig. 2b. The original diffraction peaks at 2 = 32.8°, 34.6°, 36.4° are corresponding to the reflection planes of (100), (002), and (101) of ZnO NRs. They are also well matched with the JCPDS card No. 36-1451. Furthermore, it was found that the preferred crystal orientation along (002) direction for both XRD patterns shown in Fig. 2a and b. The other two broaden diffraction peaks appeared at 2 ° = 38.4° and 44.8° are corresponding to (111) and (200) lattice planes of gold. They are corresponding to the gold nanoparticles with a face-centered cubic structure and matching the Joint Committee on Diffraction Standards (JCPDS) File No. 04-0784. The average crystallite size value of 8.2 nm of gold nanoparticles was calculated using Scherrer's formula.

The crystallite size of the gold nanostructures was calculated via Scherrer's formula (Esmaeel et al. 2010):

$$D = 0.9\lambda/\beta \cos\theta \quad (1)$$

Table 1 The calculated crystal structure parameters for ZnO NRs

Present work's results						
Sample no.	a = b (nm)	c (nm)	c/a	$D_{av.}$ (nm) Scherer's	Williamson-Hall	
					D (nm)	$\varepsilon \times 10^{-3}$
	0.3233	0.51821	1.6028	18.2	15.1	− 0.694
Reference work's results						
Wurtzite ZnO at R.T	0.32495	0.52069	1.6024	(Heller et al. 1950)		− 0.93, − 1.2
As reported in the literature	0.32535	0.52151	1.6029	(Faisal 2017;		(Zak et al. 2011)
	0.3218	0.5158	1.6028	Pearton et al. 2003; C Cui 2012)		

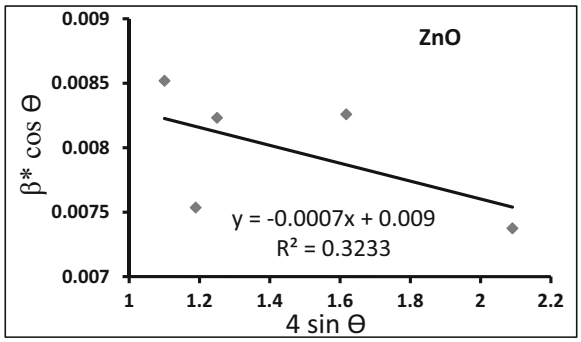

Fig. 3 The W-H plot of ZnO NRs (the strain and crystallite size are calculated from the fitting relations)

The lattice parameters (a and c) for the (100) and (002) reflection planes were calculated using formulas (2) and (3), respectively, derived from Bragg's law (Lewis 1964):

$$a = \lambda/(3)^{1/2} \tag{2}$$

$$c = \lambda/\sin\theta \tag{3}$$

The estimated values for lattice parameters are found: a = b = 3.2506 Å and c = 5.2077Å (c/a = 1.6021). These data are very close to the lattice parameters of a hexagonal wurtzite phase with pure bulk ZnO: a = 3.246 and c = 5.206 Å (Heller et al. 1950) as indicated in Table 1.

W-H plot for ZnO NRs

Williamson and Hall's plot was used to investigate the contribution of the crystallite size and strain due to the line broadening. These are represented by the so-called W-H equation (Mote et al. 2012):

$$\beta\cos\theta = k\lambda/D + 4\,\varepsilon\sin\theta \tag{4}$$

Where β is the peak broadening, λ is the X-ray wavelength, D is the crystallite size, and ε is the microstrain. The calculated results from the X-ray data for 4sinθ and βcosθ for the observed peaks of ZnO NRs with wurtzite hexagonal structure are plotted along the x- and y-axis, respectively, as shown in Fig. 3. The slope and intercept of the fitted lines have represented the strain and particle size, respectively. The negative strain values for both curves of the as-grown ZnO nanorods are due to the shrinkage in the lattice constants (mismatch between the fabric and the substrate). The low obtained strain values indicate a high-quality crystalline structure of ZnO nanorods. It is even lower than the reported values of 0.93 and 1.2 for the calcinated ZnO NPs at 750 °C and 650 °C, respectively (Zak et al. 2011). It is also found that the crystallite size values are rather small and comparable with the calculated data using Scherrer's and Williamson-Hall relations. These calculated results are summarized in Table 1. Furthermore, the high-quality crystal structure was previously confirmed by the X-ray analysis and shown in Fig. 2.

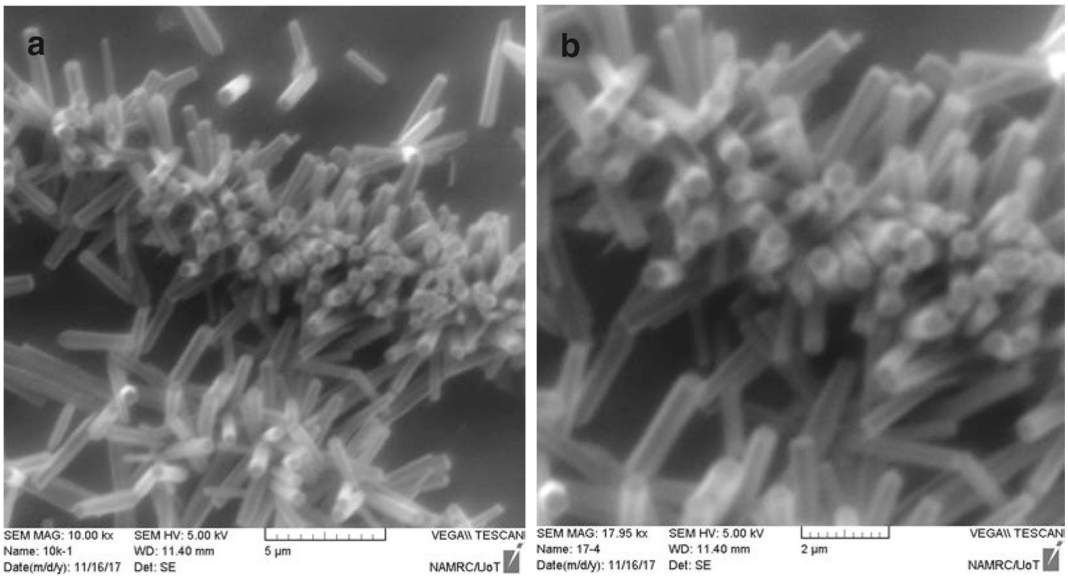

Fig. 4 SEM images of ZnO NRs on quartz substrate at different magnifications

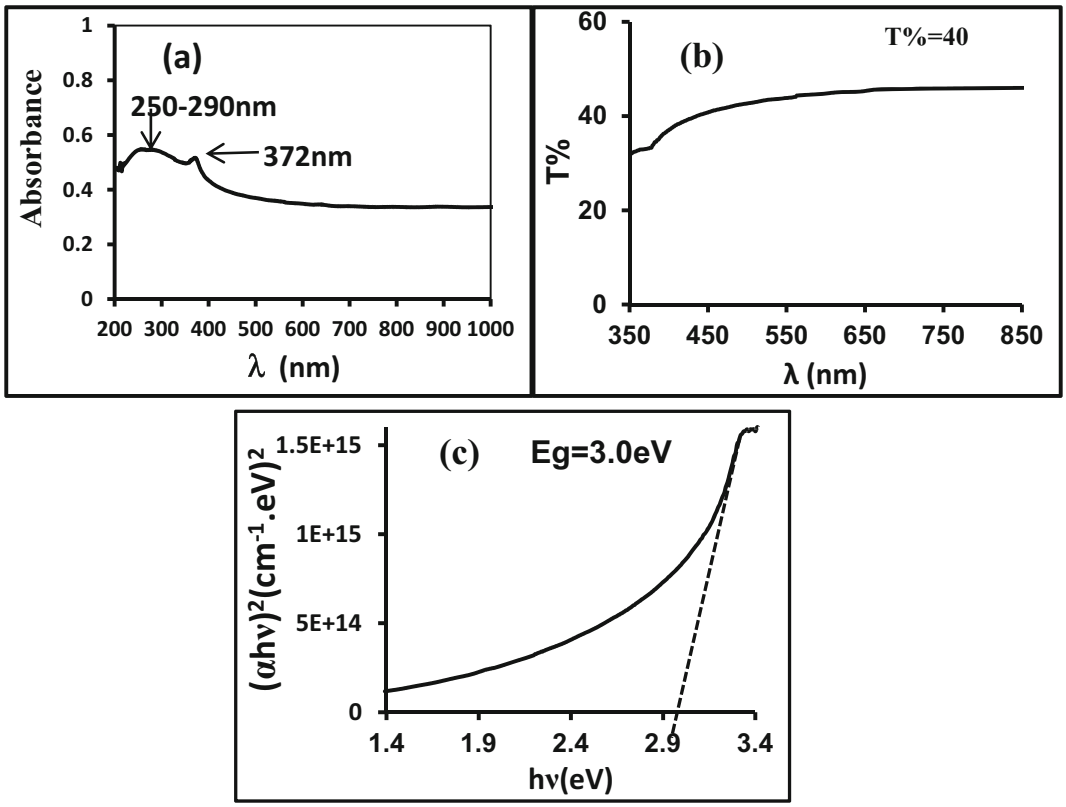

Fig. 5 Absorbance, transmittance, and energy bandgap curves of the ZnO nanostructures. **a**, **b**, and **c**, respectively

Table 1 summarizes the calculated crystal structure parameters for wurtzite ZnO at room temperature. As shown in this table, it was found that the obtained lattice constants were quite comparable to the values reported in the literature (Faisal 2017; Pearton et al. 2003; Cui 2012).

SEM analysis

Figure 4 shows typical low and high magnifications of SEM images of the as-synthesized ZnO nanostructures grown on quartz substrate using a hydrothermal route. Two different morphologies are seen due to various seed layer deposition such as spin and drop casting. Figure 4a and b show a nanorod self-assembled into flowers combined together to form semi-hierarchical nanostructures. A single flower consists of many ZnO nanorods emerging from a common point and directed toward all directions as shown in the inset of Fig. 4a. The nanorods diameters (D) are between 200 and 400 nm and 4–5 μm in length (L) with an aspect ratio (L/D) of 20–12. It

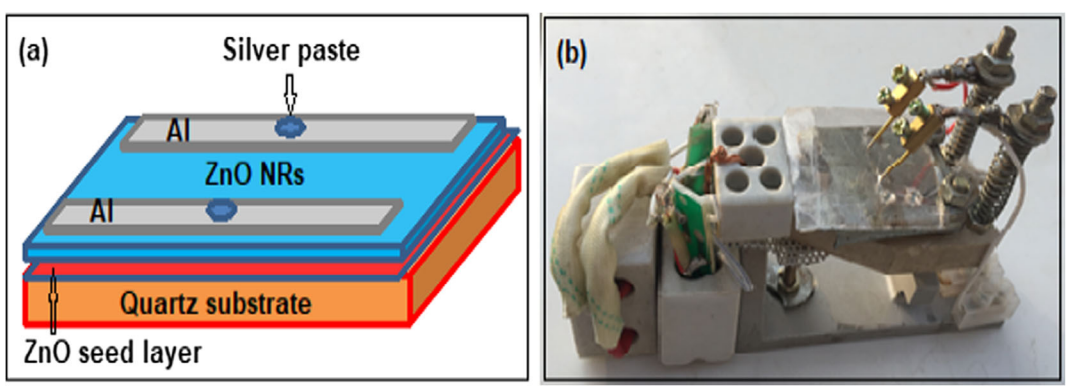

Fig. 6 Electrical and thermal measurements of ZnO NRs on quartz (**a**) and device schematic diagram (**b**) homemade two-point probe stage

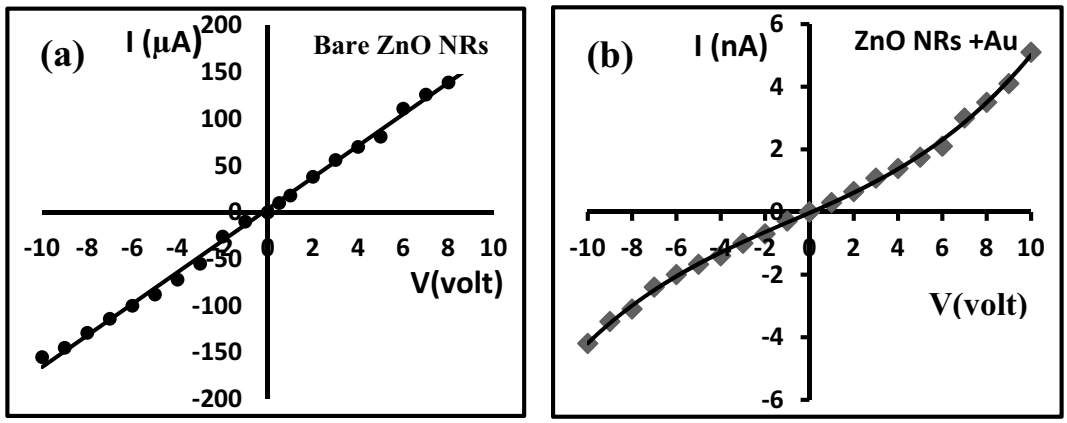

Fig. 7 Typical I-V characteristics of **a** bare ZnO NRs and **b** Au/ZnO NRs on quartz substrate at room temperature

observed the hexagonal structure of the top surface of the rods (Fig. 4b).

Optical properties of ZnO NRs

The UV-visible spectroscopy was applied to examine the visual properties of the synthesized ZnO nanostructures. Figure 5 summarizes the optical measurements for the two different nanostructures of ZnO. Figure 5a plots the absorption spectrum of the ZnO nanostructures grown on a quartz substrate in the range of 200 to 1000 nm. It can be seen, three distinguished absorption peaks, the first 1 and 2 in the UV region (250–290), and the third absorption peak is observed near the UV region at 372 nm in the UV-Vis absorbance spectrum of ZnO NRs structures, corresponds to the characteristic band of the Wurtzite hexagonal structure. It is clear that all absorption peaks of ZnO nanorods (Fig. 5a) are blue-shifted as compared to the bulk exciton absorption of ZnO (372 nm) (Zhang et al. 2001) which is due to the size effect of the nanostructures. The ZnO NRs film has a good absorption in the ultraviolet region. Therefore, in this study, the ZnO NRs film was suitable for the absorption layer of the detector application in the UV region. Figure 5b shows the result of the transmittance measurement of ZnO NRs films. It is clear from this figure that the optical transmittance of the zinc oxide nanorods sample is above 45% in the visible and NIR region (400–1100 nm). The optical bandgap energy (Eg) of a semiconductor is related to the optical absorption coefficient (α) and the incident photon energy ($h\nu$) by (Gumu et al. 2006):

$$(\alpha h\nu) = (Eg - h\nu)^n \quad (5)$$

where n depends on the kind of optical transition that prevails. Specifically, n is 1/2 and 2 when the transition is directly and indirectly allowed, respectively. The optical bandgap can be obtained by plotting the optical absorption versus the photon energy and extrapolating

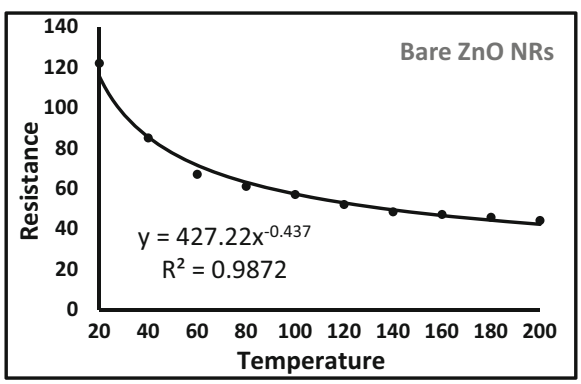

Fig. 8 Resistance versus temperature of bare ZnO NRs

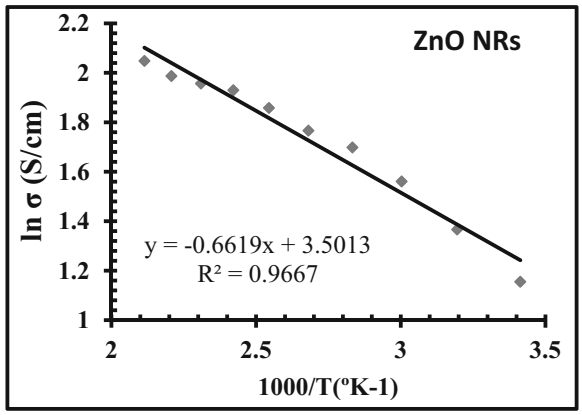

Fig. 9 Arrhenius plot of ZnO film

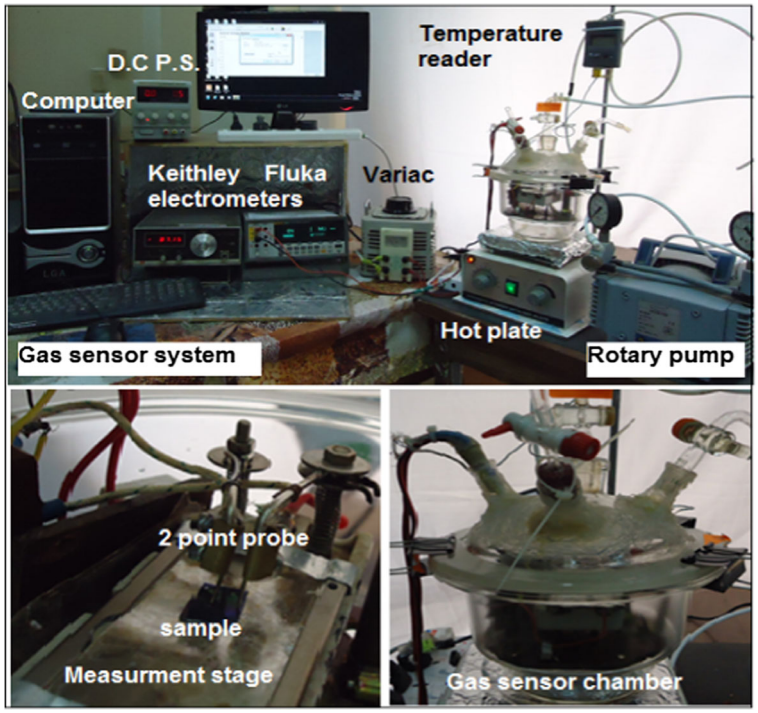

Fig. 10 Photograph of a homemade gas sensor system

the linear portion of the curve to $(\alpha h\nu)^2 = 0$. Figure 5c shows the variation of $(\alpha h\nu)^2$ versus photon energy ($h\nu$) for ZnO NRs on quartz substrates. It is readable from this shape that the optical gap of zinc oxide was found to be 3.0 eV, which is smaller than the bulk value of 3.31 eV (Oktik 1988), and quite well met with previously reported data of ZnO thin film (Paraguay et al. 1999).

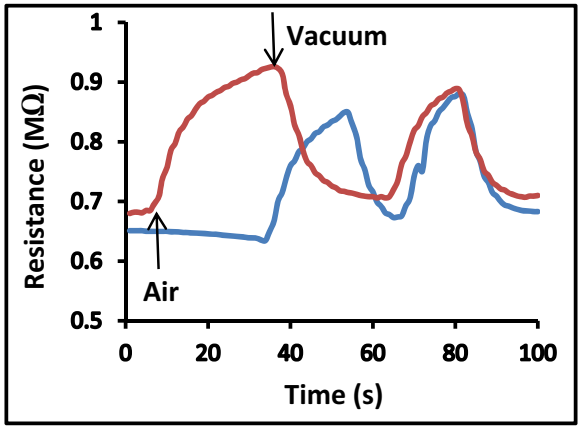

Fig. 11 Typical adsorption-desorption process of bare ZnO NRs film at room temperature

Electrical and thermal properties

The ZnO NRs sensor device is fabricated as shown in Fig. 6a. Aluminum electrodes for measurements were evaporated on the sensing material. A spot of silver paste was made on the top of aluminum electrodes. The electrical and thermal parameters of the sensor device were carried on by using the homemade measurement stage shown in Fig. 6b. This stage consists of a miniature metal plate with a heater and thermocouple for temperature measurements. Two adjustable point probes made of gold-coated pins were used for the measurements. These probes were fixed on the top of silver spots.

I-V characteristic of ZnO NRs on quartz

Figure 7 shows the plot of the current to voltage curve of ZnO NRs on the quartz substrate at room temperature. It was observed that the I-V curve of the bare ZnO NRs film is linear and obeys ohms law as shown in Fig. 7a, so that the contact between the ZnO film and the Al is ohmic. The other curve shown in Fig. 7b of ZnO NRs with Au slightly deviated from ohm's law. This could be attributed to the presence of gold nanoparticles, which

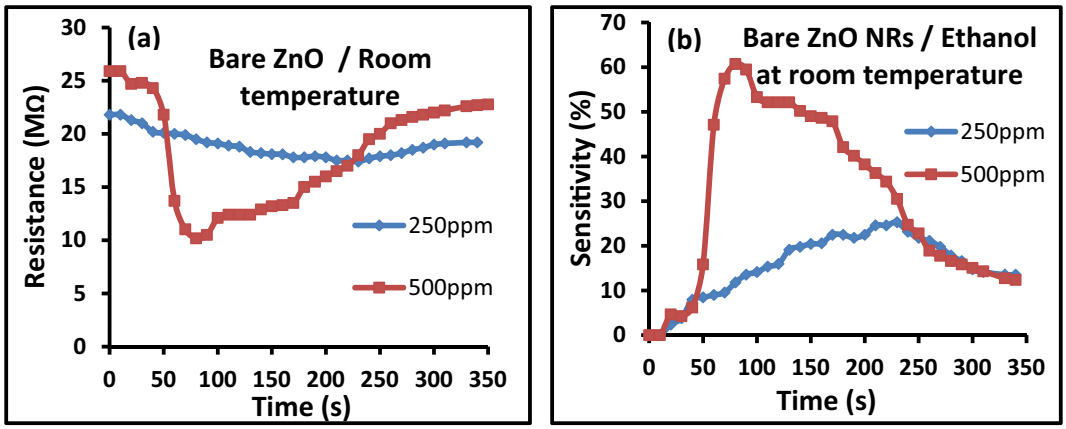

Fig. 12 Room temperature resistance response (**a**) and sensitivity (**b**) of bare ZnO NRs at ethanol concentrations of 250 ppm and 500 ppm

can create a Schottky barrier. These properties could affect the sensing performance, especially at room temperature.

Thermal resistance measurements

The electrical resistance of ZnO NRs on quartz substrate samples was measured as a function of temperature variation in the range of 20–200 °C as shown in Fig. 8. It was observed that the resistance decreases with an increase in temperature and indicates its semiconductor behavior. The fitting formula for the sample was obtained and represented by a power law (Fig. 8). The resistance to temperature variation is 432 Ω/°C. Such a large variation in the resistance indicates the greater sensitivity of the presence sensing element.

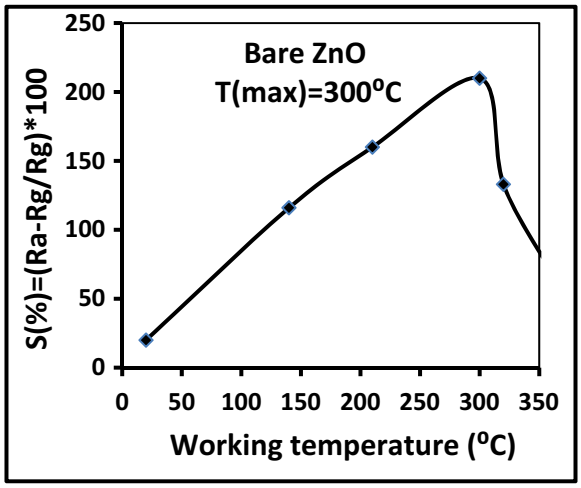

Fig. 13 Sensitivity versus temperature of bare ZnO NRs at 500 ppm of ethanol vapor

Activation energy calculation

The activation energy for n-type semiconductor materials is defined as a measure of the thermal or another form of energy required to raise the electron from the donor level (E_d) to the conduction band (E_c). This corresponds to the energy difference ($E_c - E_d$). The resistance variation as a function of temperature is represented by Eq. 6 (Frank and Köstlin 1982):

$$R = R_o \exp\left(-\Delta E/2kT\right) \tag{6}$$

Rewritten of Eq. 6 in the form:

$$\ln R = \ln\left(R_o\right) - \left(\Delta E/2kT\right) \tag{7}$$

where R = resistance, R_o = constant, ΔE = activation energy, k = Boltzmann's constant, and T = absolute temperature.

The activation energy was calculated from the Arrhenius plot of ln S versus ln 1/T graph and is shown in Fig. 9. This plot gives a value of $E_a = 0.0571$ in a temperature range of 20–200 °C. This minimum value of activation energy is quite significant for gas sensors operating at room temperature.

Gas sensor fabrication

The gas sensing device was fabricated based on ZnO NRs film on quartz substrate as shown in Fig.6a. Two aluminum electrodes on ZnO film were deposited via physical vapor evaporation (PVD) technique. This device was fixed on the measurement stage shown in Fig. 6b and located inside the gas chamber as shown in Fig. 10.

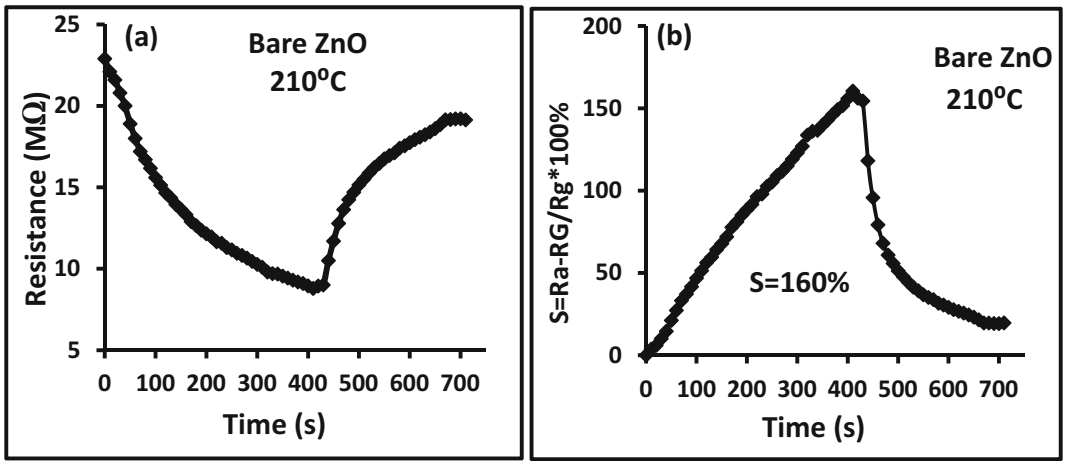

Fig. 14 Typical sensor response of bare ZnO NRs at 210 °C and 500 ppm of ethanol. **a** Sensor response curve and **b** sensitivity versus time

Adsorption-desorption processes

Figure 11 demonstrates the reproducible sensing response during two adsorption-desorption cycles without ethanol by switching from the air at ambient pressure to vacuum at 100 mTorr. The resistance increased when air is admitted to the chamber forming adsorption of oxygen molecules on the surface and then decreased during the pumping process which is due to the desorption of the oxygen molecules at the surface of the ZnO NRs film. This process was found to be reproducible for adsorption-desorption of the sensor response as shown in the two curves (red and blue curves). These properties give us an indication of the successful behavior of ZnO NRs film for gas sensing. Moreover, the adsorption of oxygen molecules on the ZnO NRs surface can be described elsewhere (Beatriz et al. 2017). The adsorption of these oxygen species on the surface of ZnO NRs, capturing electrons from the conduction band and the associated decrease in the charge carrier concentration (e^-), leads to an increase in the resistance of the n-type ZnO until it attains equilibrium. Thus, the surface resistance increases and attains equilibrium during the chemisorption process.

Static response of conductometric measurements

Conductometric measurements were performed on the sensor of the ZnO nanostructure film using the static technique. The essential procedure of such kind of

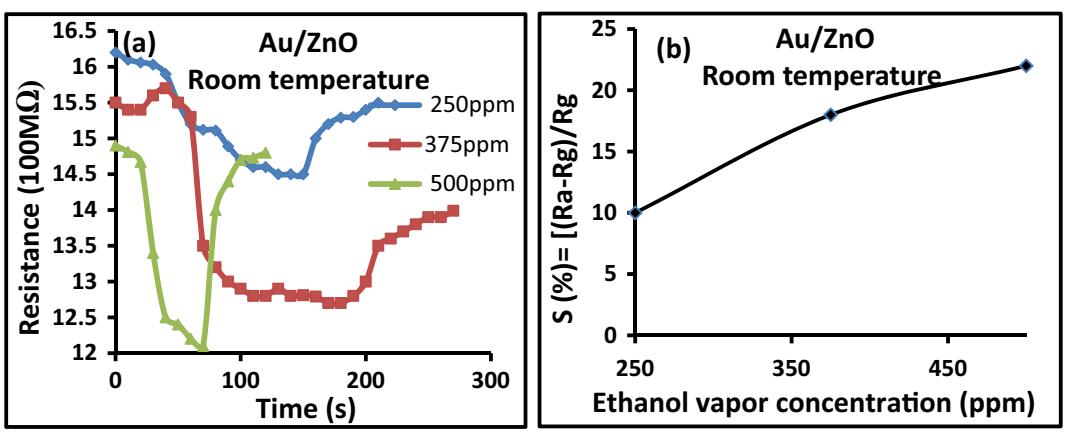

Fig. 15 **a** Resistance response of gold-decorated ZnO NRs at room temperature. **b** Sensitivity versus ethanol vapor concentrations

measurements depends on the resistance variation. The change in the resistance was observed upon exposure to the target gas relative to the resistance in the air. This behavior could be observed for the n-type semiconductor sensor device toward oxidizing and reducing gases. In the present work, the relative sensitivity ($S\%$) for ethanol vapor is defined as follows (Rafaela et al. 2018):

$$S = \left[\left(R_a - R_g\right)/R_g\right] \times 100\% \quad (8)$$

where R_a is the resistance in the air and R_g is the resistance at ethanol vapor.

Gas sensor performance

Sensor measurements of bare ZnO NRs

The sensor measurements of bare ZnO NRs at room temperature toward 250 ppm and 500 ppm of ethanol vapor are shown in Fig 15. The resistance response versus time and its sensitivity curves are shown in Fig. 12a and b. Low sensitivity can be observed at 250 ppm of ethanol concentration ($S = 20\%$) compared with the value at 500 ppm (60%), which is relatively higher.

The sensitivity of bare ZnO NRs was calibrated versus the working temperature of the fixed ethanol vapor of 500 ppm as shown in Fig. 13. The operating temperature was deduced from the maximum sensitivity. This value is equal to 300 °C which represents the operating temperature.

The typical resistance response versus time and its corresponding sensitivity of bare ZnO NRs at 500 ppm of ethanol vapor and at high temperature (210 °C) are shown in Fig. 14. The estimated value of the sensitivity ($S = 160\%$) confirms the influence of the heating on the sensor's performance.

Sensor measurements of Au-decorated ZnO NRs

The sensor measurements were conducted on the gold-decorated ZnO NRs film at room temperature toward 250, 275, and 500 ppm of ethanol vapor concentrations. The resistance response versus time and the corresponding sensitivity curves are shown in Fig. 15. The sensitivity values in the range of 10–20% can be determined from Fig. 15b. They are reasonably low sensitivity values even at higher ethanol concentration.

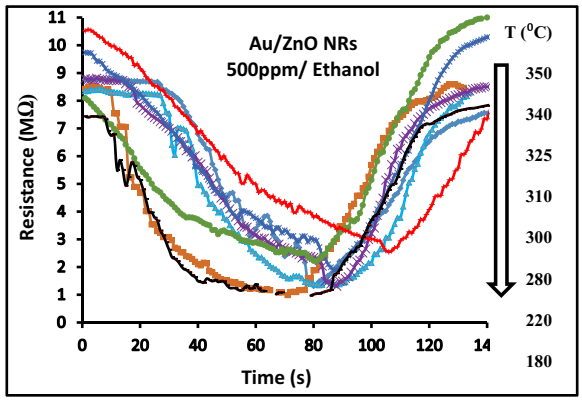

Fig. 16 Sensor response curves of Au-decorated ZnO NRs at various temperatures with 500 ppm of ethanol vapor

The resistance response versus time of Au-decorated ZnO NRs sensor was also investigated at several temperatures and a fixed ethanol vapor concentration of 500 ppm. This is clearly shown in Fig. 16 and it can be seen that the resistance was decreased when the temperature decreased in the presence of ethanol vapor. The sensitivity versus the working temperature at a fixed ethanol vapor concentration of 500 °C was calibrated and drawn in Fig. 17. In this case, the operating temperature was estimated within 325 °C at a maximum sensitivity value of about 700%. This high sensitivity value at higher ethanol vapor concentration of 500 ppm shown in Fig. 18a confirmed the influence of the sensor's heating. So, the sensitivity results are quite higher for the Au-decorated ZnO NRs compared with the sensitivity results of the bare ZnO NRs even at high operating

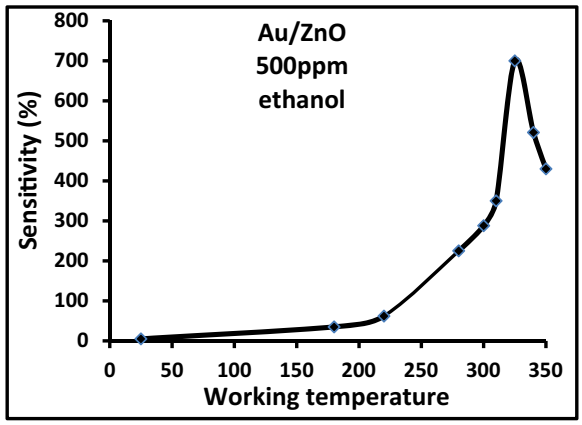

Fig. 17 Sensitivity versus temperature of gold-decorated ZnO NRs film at several temperatures at 500 ppm of ethanol vapor

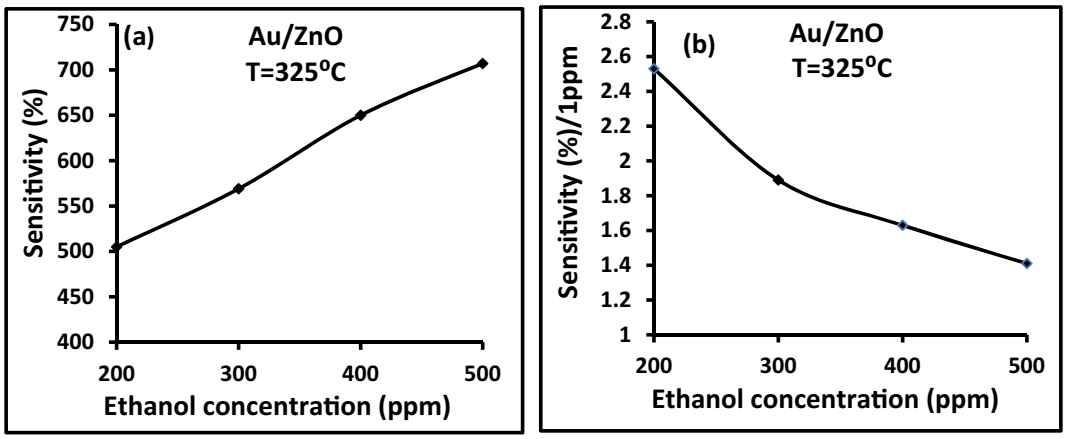

Fig. 18 **a** Relative sensitivity (*S*%) and **b** sensitivity (S%/1 ppm) versus ethanol concentration of gold-decorated ZnO NRs at 325 °C

temperatures. This sensitivity enhancement can be attributed to the increase of the oxygen species interacting with the sensor's material surface at high temperatures. Finally, Fig. 18b shows the response per unit concentration versus ethanol vapor concentration.

Sensor's evaluations

The evaluation of the sensors was based on the data tabulated listed in Table 2. The average sensitivity (response per unit concentration) at room temperature for a sample of Au-decorated ZnO NRs was calculated: $S\%/1\ \text{ppm} = 0.044 \pm 0.004\%/1\ \text{ppm}$. This value could be compared with the minimum value of sensitivity at 325 °C, which is equal to 0.07%/1 ppm. Also the ratio of the max value at 325 °C divided by the value at room temp = 1.4%/1 ppm divided by 0.044%/1 ppm = 32 times. This means that the sensitivity of ZnO NRs coated with gold was enhanced 32 times compared with the room temperature value obtained for the same sample.

Conclusion

ZnO NRs on quartz substrates were successfully synthesized via hydrothermal route.

The characterized materials by using XRD, SEM, and UV confirmed the formation of single-crystalline ZnO nanorods on quartz. The bare ZnO NRs and gold-decorated ZnO NRs were separately fabricated as an ethanol gas sensor at a concentration of 500 ppm and room temperature. It was found that the sensor decorated with gold shows an enhanced sensor response compared with the bare ZnO NRs at room temperature. The optimum operating temperature of the sensor decorated

Table 2 The sensitivity results for bare ZnO NRs and Au-decorated ZnO NRs at 500 ppm of ethanol concentration

Sensitivity (*S*%)	Bare ZnO NRs		Au/ZnO NRs sputtered coating with 50 nm	
	Ethanol concentration = 500 ppm			
Operating temperature	Room temperature	300 °C	Room temperature	325 °C
$(R_a - Rg / R_g) \times 100\%$	60–90%	210%	22%	700%
S%/1 ppm	0.12–0.18	0.42	0.044	1.4
Sensitivity ratio	0.42/0.12 = 3.5 0.42/0.18 = 2.3		1.4/0.044 = 32	
Resistance range	10^8–10^9 Ω (Low conductivity)		10^6 Ω (High conductivity)	

with gold at a concentration of 500 ppm of ethanol was 325 °C. The obtained sensitivity for Au-decorated ZnO NRs was found to sustain good working performance toward ethanol vapor at 325 °C. Hence, the sample of ZnO NRs decorated with gold nanoparticles can be used as a good sensing device toward ethanol gas.

Compliance with ethical standards

Conflict of interest The authors declare that they have no conflict of interest.

References

Alaie Z, Mohammad NS, Yousefi MH, Safarzadeh S (2016) The effect of different seed layers and growth time on the quality of ZnO NRs arrays. Int J Nanosci Nanotechnol 12:119–130

Alejandro E-M, Rubén A-G, Ernesto C-A, Armando P-C, Antonio M-B, Carlos A-T (2016) ZnO micro- and nanostructures obtained by thermal oxidation: microstructure, morphogenesis, optical, and photoluminescence properties. Crystals 6: 135. https://doi.org/10.3390/cryst6100135

Ayesha NUH, Akhtar N, Ikram U, Ghulam M, Masoom Y, Imran K (2017) Synthesis approaches of zinc oxide nanoparticles: the dilemma of ecotoxicity. J Nanomater 2017:8510342 14 pages. https://doi.org/10.1155/2017/8510342

Beatriz AV, Cecilia AZ, Tarcisio MP, Diogo PV (2017) ZnO nanorods/graphene oxide sheets prepared by a chemical bath. J Alloys Compd 696:996–1003. https://doi.org/10.1016/j.jallcom.2016.12.075

Benoit NI, Amy CC, Stefan S, Raffaello DC, Tim SJ, Sandrine H, Martyn AM, David WM, Riley DJ, Mary PR (2011) Electrodeposition of ZnO layers for photovoltaic applications: controlling film thickness and orientation. J Mater Chem 21:12949–12957. https://doi.org/10.1039/C1JM11225Bh

Changlei X, Shichao Z, Shengbin W et al (2016) ZnO nanoparticles encapsulated in a 3D hierarchical carbon framework as anode for lithium-ion battery. Electrochim Acta 189:245–225. https://doi.org/10.1016/j.electacta.2015.11.045

Cui J (2012) Zinc oxide nanowires. Mater Charact 64:43–52. https://doi.org/10.1016/j.matchar.2011.11.017

Doungporn Y, Kanittha B, Wiyong K (2009) Preparation of ZnO nanostructures by solvothermal method. J Micros Soc Thai 23:75–78

Esmaeel D, Mohammad R, Fereshteh B (2010) One-step synthesis of maghemite (γ-Fe_2O_3) nanoparticles by a wet chemical method. J Alloys Compd 502:257–260. https://doi.org/10.1016/j.jallcom.2010.04.163

Faisal AD (2016) Optimization of CVD parameters for long ZnO NWs grown on ITO/glass substrate. Bull Mater Sci 39:1635–1643. https://doi.org/10.1007/s12034-016-1316-6

Faisal AD (2017) Synthesis of ZnO comb-like nanostructures for high sensitivity H_2S gas sensor fabrication at room temperature. Bull Mater Sci 40:1061–1068

Frank G, Köstlin H (1982) Electrical properties and defect model of tin-doped indium oxide layers. Appl Phys A 27:197–206. https://doi.org/10.1007/BF00619080

Giri PK, Patel PK, Panchal CJ, Bhattacharyya S, Kumari S, Singh DK, Desai MS (2007) Studies on zinc oxide nanorods grown by electron beam evaporation technique. Synth Reactivity Inorg Metal-Organic Nano-Metal Chem 37:437–441. https://doi.org/10.1080/15533170701466018

Gumu C, Ozkendir OM, Kavak H, Ufuktepe Y (2006) Structural and optical properties of zinc oxide thin films prepared by spray pyrolysis method. J Optoelectron Adv Mater 8:299–303 https://www.researchgate.net/publication/280137343

Hamed M, Majid D (2017) Zinc oxide nanoparticles. Biological synthesis and biomedical applications. Ceram Int 43:907–914. https://doi.org/10.1016/j.ceramint.2016.10.051

Hasnidawani JN, Azlina HN, Norita HN, Bonnia NN, Ratim S, Ali ES (2016) Synthesis of ZnO nanostructures using sol-gel method. Procedia Chem 19:211–216. https://doi.org/10.1016/j.proche.2016.03.095

Heller RB, McGannon J, Weber AH (1950) Precision determination of the lattice constants of zinc oxide. J Appl Phys 21: 1283–1284. https://doi.org/10.1063/1.1699591

Huanming M, Zhiwei Q, Zaide W, Ahmad M et al (2017) Enhanced field emission of ZnO nanoneedle arrays via solution etching at room temperature. Mater Lett 206:162–165. https://doi.org/10.1016/j.matlet.2017.07.014

Husam SA, Abdullah MJ (2015) Preparation of ZnO nanostructures by RF-magnetron sputtering on thermally oxidized porous silicon substrate for VOC sensing application. Measurement 59:248–257. https://doi.org/10.1016/j.measurement.2014.08.011

Jimenez-Cadena G, Comini E, Ferroni M, Vomiero A, Sberveglieri G (2010) Synthesis of different ZnO nanostructures by a modified PVD process and potential use for 1dye-sensitized solar cells. Mater Chem Phys 124:694–698. https://doi.org/10.1016/j.matchemphys.2010.07.035

Kołodziejczak-Radzimska A, Jesionowski T, Krysztafkiewicz A (2010) Obtaining zinc oxide from aqueous solutions of KOH and $Zn(CH_3COO)_2$. Physicochem Probl Miner Process 44: 93–102

Lewis K (1964) X-ray diffraction in crystals, imperfect crystals, and amorphous bodies. J Chem Educ 41:292. https://doi.org/10.1021/ed041p292.2

Lin JC, Lee CP, Ho KC (2012) Zinc oxide synthesis via a microemulsion technique: morphology control with application to dye-sensitized solar cells. J Mater Chem 22:1270–1273. https://doi.org/10.1039/C1JM15227K

Lv H, Sang DD, Li HD, Du XB, Li DM, Zou GT (2010) Thermal evaporation synthesis and properties of ZnO nano/microstructures using carbon group elements as the reducing agents. Nanoscale Res Lett 5:620–624. https://doi.org/10.1007/s11671-010-9524-2

Mohamad HM, Tetsuo S, Mohamad RM (2015) Humidity sensor-a review of nanostructured zinc oxide (ZnO) –based humidity sensor. Adv Mater Res 1109:395–400. https://doi.org/10.4028/www.scientific.net/AMR.1109.395

Mohammad K, Vahedi V, Reyhani A (2012) Synthesis and characterization of ZnO nanowires by thermal oxidation of Zn

thin films at various temperatures. Molecules 17:5021–5029. https://doi.org/10.3390/molecules17055021

Mote VD, Purushotham Y, Dole BN (2012) Williamson-hall analysis in estimation of lattice strain in nanometer-sized ZnO particles. J Theor Appl Phys 6:1–6 http://www.jtaphys.com/content/2251-7235/6/1/6

Muchuweni E, Stephen ST, Hyggins N (2017) Synthesis and characterization of zinc oxide thin films for optoelectronic applications. Heliyon 3:1–16. https://doi.org/10.1016/j.heliyon.2017.e00285

Muhammad H, Hongyu S, Shafqat K, Amjad N, Maaz K, Anwar UH, Munawar I, Mashkoor A (2016) Noble metal nanoparticle-functionalized ZnO nanoflowers for photocatalytic degradation of RhB dye and electrochemical sensing of hydrogen peroxide. J Nanopart Res 18:1–14. https://doi.org/10.1007/s11051-016-3397-y

Oktik S (1988) Low cost, non-vacuum techniques for the preparation of thin/thick films for photovoltaic applications. Prog Cryst Growth Charact 17:171–240. https://doi.org/10.1016/0146-3535(88)90006-8

Paraguay F, Estrada W, Acosta DR, Andrade E, Yoshida MM (1999) Growth, structure and optical characterization of high-quality ZnO thin film obtained by spray pyrolysis. Thin Solid Films 350:192–202. https://doi.org/10.1016/S0040-6090(99)00050-4

Pearton SJ, Norton DP, Ip K, Heo YW, Steiner T (2003) Recent progress in processing and properties of ZnO. Superlattices Microst 34:3–32. https://doi.org/10.1016/S0749-6036(03)00093-4

Rafaela DS, Dongwook K, Qiuchen D, Wai Y, Daniel SC, Luiz HCM, Yu L (2018) Sensitive and selective NH_3 monitoring at room temperature using ZnO ceramic nanofibers decorated with polystyrene sulfonate. Sensors 18:1–13. https://doi.org/10.3390/s18041058

Rajesh K, Girish K, Ahmad U (2014) Pulse laser deposited nanostructured ZnO thin films: a review article. J Nanosci Nanotechnol 14:1911–1930. https://doi.org/10.1166/jnn.2014.9120y

Richa S (2013) Temperature sensor based on nano-sized zinc oxide synthesized via dropwise method. Int J Pure Appl Sci Technol 14:9–15 https://pdfs.semanticscholar.org/24e3/a7b67dec4efebcf5e2d91516d3b2d10a4b2f.pdf

Salvatore C, Giorgia F, Vincenzina S, Kuo-Juei H, Ting-Wei L, Nofar MH, Salvo M, Didier G, Peter L, Yosi S-D (2017) Role of AuxPt1–x clusters in the enhancement of the electrochemical activity of ZnO nanorod electrodes. J Phys Chem C 121:15644–15652. https://doi.org/10.1021/acs.jpcc.7b00480

Shi W, Song S, Zhang H (2013) Hydrothermal synthetic strategies of inorganic semiconducting nanostructures. Chem Soc Rev 42:5714–5743. http://pubs.rsc.org. https://doi.org/10.1039/C3CS60012B

Xiaohong X, Kangzhe C, Yijing W, Jiao Lifang J (2016) 3D hierarchical porous ZnO/$ZnCo_2O_4$ nanosheets as high-rate anode material for lithium-ion batteries. J Mater Chem A 4:6042–6047. https://doi.org/10.1039/c6ta00723f

Yang K, She GW, Wang H, Ou XM, Zhang XH, Lee CS, Lee ST (2009) ZnO nanotube arrays as biosensors for glucose. J Phys Chem C 113:20169–20172. https://doi.org/10.1021/jp901894j

Yangyang Z, Manoj KR, Elias KS, Yogi GD (2012) Synthesis characterization, and applications of ZnO nanowires. J Nanomater 12:1–22. https://doi.org/10.1155/2012/624520

Yuhai S, Limin C, Yunfeng B, Yujun Z, Jing W, Mingli F, Junliang W, Daigi Y (2016) The applications of morphology-controlled ZnO in catalysis. Catalysts 6:1–44. https://doi.org/10.3390/catal6120188

Zak AK, Majid WA, Abrishami ME, Yousefi R (2011) X-ray analysis of ZnO nanoparticles by Williamson–hall and size–strain plot methods. Solid State Sci 13:251–256. https://doi.org/10.1016/j.solidstatesciences.2010.11.024

Zhai B, Huang Y-M (2016) A review on recent progress in ZnO based photocatalysts. Opt Mater 1:22–36 https://www.sciencedirect.com/science/article/pii/S1878535216301058

Zhang SB, Wei S-H, Alex Z (2001) Intrinsic n-type versus p-type doping asymmetry and the defect physics of ZnO. Phys Rev B Condens Matter B 63:075205–7. https://doi.org/10.1103/PhysRevB.63.075205

Zhiwei S, Amy VW (2015) Chemical Bath deposition of ZnO on functionalized self-assembled monolayers: selective deposition and control of deposit morphology. Langmuir 31:1421–1428. https://doi.org/10.1021/la5040239